ISSN 0021-3640, JETP Letters, 2024, Vol. 120, No. 1, pp. 56–65. © Pleiades Publishing, Ltd., 2024.
Russian Text © The Author(s), 2024, published in Pis'ma v Zhurnal Eksperimental'noi i Teoreticheskoi Fiziki, 2024, Vol. 120, No. 1, pp. 51–61.

CONDENSED MATTER

Features of the Response of Majorana Quasiparticles in Superconducting Wires (Brief Review)

S. V. Aksenov*

Kirensky Institute of Physics, Federal Research Center KSC, Siberian Branch, Russian Academy of Sciences, Krasnoyarsk, 660036 Russia

**e-mail: asv86@iph.krasn.ru*

Received April 12, 2024; revised June 6, 2024; accepted June 8, 2024

Interest in hybrid quasi-one-dimensional systems with an inner semiconducting part coated with a superconductor (the so-called core/shell structure) has been grown in the last decade. Materials with a strong spin–orbit coupling and a large *g*-factor (InAs, InSb) are chosen as semiconductors. Due to the proximity effect, such objects can be considered as superconducting wires, where the existence of Majorana states has been predicted. This review briefly summarizes the current experimental studies aimed at the detection of Majorana quasiparticle excitations in superconducting wires. Furthermore, prospects of using the interference geometry of devices including such wires are discussed. In particular, the coherent transport in a spatially inhomogeneous one-dimensional normal metal/superconductor/normal metal system, where normal metal wires serve as arms of an interference device, which interact with a normal metal contact, has been analyzed theoretically. It has been found that responses of Majorana and Andreev low-energy excitations of the device can be distinguished.

DOI: 10.1134/S0021364024601192

1. INTRODUCTION

The properties of the ground state and low-energy excitations of a chain of spinless fermions, which consists of N sites and is characterized by the hopping, $t > 0$, and p-type superconducting pairing, Δ, parameters between nearest neighbors and by the chemical potential μ, were studied in [1]. It was found that a Bogoliubov excitation with the energy decreasing exponentially with increasing chain length, i.e., $\varepsilon_1 \sim e^{-L/\xi}$, where $\xi \sim \Delta^{-1}$ is the coherence length and $L = Na$ is the chain length (below, $a = 1$), is implemented in an open system at $|\mu| < 2t$. In other words, a zero-energy edge state appears at $L \gg \xi$. The bulk spectrum of this system, which is often called the Kitaev wire or chain, with periodic boundary conditions is gapped:

$$\varepsilon_k = \sqrt{(2t\cos k + \mu)^2 + 4\Delta^2 \sin^2 k}. \qquad (1)$$

According to Eq. (1), the gap at $\mu = \pm 2t$ is closed if the wave vector is $k = \pi, 0$. Thus, the appearance of the edge state in the chain with open boundary conditions under the continuous variation of the parameters is accompanied by a quantum phase transition in the system with periodic boundary conditions.

The specificity of the appearing edge state becomes obvious after the transition from the second quantization Fermi operators at the jth site c_j, c_j^+, to the Majorana operators $\gamma_{Aj} = c_j + c_j^+$, $\gamma_{Bj} = i(c_j^+ - c_j)$, and $\gamma_{A,Bj} = \gamma_{A,Bj}^+$. Similarly, the operator of any Bogoliubov excitation α_n ($n = 1,\ldots,N$) in the space of eigenstates of the Bogoliubov–de Gennes Hamiltonian can be represented as the superposition of Majorana mode operators $\alpha_n = (b_{1n} + ib_{2n})/2$ and $b_{1,2n} = b_{1,2n}^+$. As a result, it is easy to show that any excitation satisfies the relation

$$b_{1n} = \sum_j w_{jn}\gamma_{Aj}, \quad b_{2n} = \sum_j z_{jn}\gamma_{Bj}, \qquad (2)$$

where the coefficients $w_{jn} = u_{jn} + v_{jn}$ and $z_{jn} = u_{jn} - v_{jn}$ can be interpreted as the values of the wavefunctions of Majorana modes of the nth excitation at the jth site. They are expressed in terms of the Bogoliubov uv coefficients; i.e., $c_j = \sum_n (u_{jn}\alpha_n + v_{jn}\alpha_n^+)$.

If the on-site energy measured from the chemical potential μ is zero and $|\Delta| = t$, the lowest-energy excitation has zero energy $\varepsilon_1 = 0$ and $b_{1,1} \equiv b_1 = 2u_{1,1}\gamma_{A1}$, $b_{2,1} \equiv b_2 = 2u_{N,1}\gamma_{BN}$, and $u_{1,1} = u_{N,1}$. At the deviation from the symmetric point $|\Delta| = t$, $\mu = 0$, the wavefunctions of Majorana modes are hybridized, which generally leads to a nonzero energy of the excitation ε_1, which, as mentioned above, decreases exponentially with increasing N and is an oscillatory function of the

energy parameters of the system. The state with a nearly zero energy and constituent Majorana modes localized at opposite ends is called the Majorana state. It is noteworthy that the Majorana state (MS) is a particular case of an Andreev state (AS)—a superposition of the electron and hole waves with the energy inside the gap—appearing in systems with a spatially inhomogeneous superconducting pairing potential [2].

The chain with the MS is considered as the system in the topological superconductivity phase in view of a nontrivial topology of the space of Bloch wavefunctions $\psi_n(k)$. Indeed, the Berry phase acquired at the motion over the Brillouin zone is [3, 4]

$$\gamma = \int_{-\pi}^{\pi} dk \sum_n \left(\psi_n^*(k), \frac{\psi_n(k)}{dk} \right) = \begin{cases} 0, & |\mu| > 2t; \\ \pi, & |\mu| < 2t. \end{cases} \quad (3)$$

The phase γ is related as $M = \exp(i\gamma)$to the Majorana number M, which is a topological invariant proposed in [1].

Majorana quasiparticles are not only of fundamental interest due to their exotic properties. For several reasons, Majorana modes can possibly be used in quantum computing. The existence of zero-energy excitation indicates the double degeneracy of the ground state, which has indefinite parity. As a result, the evolution of the wavefunction of a qubit can be considered in the basis of two such states $|0\rangle$ and $\alpha_0^+|0\rangle$ [5, 6]. The authors of [7] showed that a change in the wavefunction of the qubit that is not reduced to the multiplication by a global phase factor can be ensured by interchanging the Majorana modes b_1 and b_2 in a T-shaped wire without the closure of the gap in the bulk spectrum (i.e., performing the braiding operation). The latter occurs because Majorana fermions are non-Abelian anions [8]. Another feature of the MS important for applications is its nonlocal character. As a result, the MS is topologically protected against local perturbations [9, 10], including decoherence processes, which constitute an obvious stumbling block for the fabrication of nontopological qubits.

A more realistic one-dimensional model was proposed in [11, 12] to describe a semiconducting wire with the Rashba spin–orbit coupling on the surface of an *s*-wave superconductor in a magnetic field. Since superconducting pairing characterized by the gap Δ occurs in the wire itself due to the proximity effect, this wire is referred to below as the superconducting wire. A nontrivial phase in such a system is implemented if the Zeeman energy h is above the threshold value h_c; in the continuum approximation, $h > \sqrt{\mu^2 + \Delta^2}$.

At $\Delta = 0$, the spin–orbit coupling with the intensity α and Zeeman splitting lead to the formation of two band of helical states separated by the gap h at $k = 0$ [13]. Then, the projection of the Hamiltonian of the original model on the subspace of the bottom-band states at $\Delta \neq 0$ and $h, |\mu| \gg t, \alpha, \Delta$ (where t is the hopping parameter in the tight-binding approximation) gives the Hamiltonian of the Kitaev model, where the fermion pairing intensity is $\sim\alpha\Delta/h$ [11, 14]. Thus, the *s*-wave pairing dominates in the superconducting wire at $h < h_c \approx |\mu|$, while the effective *p*-wave superconductor is implemented at $h \gtrsim |\mu|$ [15].

In several years after the cited theoretical proposals, first local tunneling spectroscopy studies of the transport properties of a hybrid semiconductor/superconductor wire were carried out [16–18]. Researchers often choose InAs (InSb) semiconductor wires, which have a large Rashba parameter $\alpha_R = 0.2$–0.8 eV Å (0.2–1 eV Å), high *g*-factor $g = 8$–15 (40–50), and a small effective mass $m^* = 0.023m_e$ ($0.014m_e$) [19]. In the first works, a semiconductor wire was placed on the surface of a massive Al or NbTiN superconductor. A technology of the epitaxial growth of a superconducting layer on the surface of a semiconductor core (so-called core/shell structure) was later developed. The gap in the core reached due to the proximity effect is $\Delta = 0.2$–1 meV. Correspondingly, structures are experimentally studied at temperatures $T \sim 0.01$–0.1 K in magnetic fields of $B \sim 1$ T. In view of a negative effect of the magnetic field on superconducting pairing, some recent experiments were performed with hybrid wires with a EuS magnetic insulator layer deposited in addition to the superconducting layer [20–22].

It is worth noting that a significant technological progress in the growth of hybrid wires, the improvement of the parameters of the semiconductor/superconductor interface, etc. was achieved in about a decade after the beginning of experiments. This results in the detection of the following theoretically predicted effects of transport in the MS: the appearance of a quantized peak of the differential conductance at zero voltage [23, 24] and its stability under the variation of the tunnel barrier height at the normal metal/superconducting wire interface, Zeeman energy, chemical potential, and the presence of disorder [25].

It is known that electrons with the energy inside the gap of the superconductor that are incident on the superconductor from the normal metal undergo local Andreev reflection at the interface [26]. If the Fermi level is in the center of the gap and a Majorana mode is localized at the edge of the superconductor, Andreev reflection processes become resonant at any value of the tunnel integral. As a result, the conductance at zero bias voltage has a maximum with the height $2G_0$. Here, $G_0 = e^2/(2\pi\hbar)$ is the conductance quantum, where $\hbar$ is the reduced Planck constant, and a factor of 2 indicates the presence of electron and hole degrees of freedom rather than spin degeneracy [23, 27].

A transition to a topologically nontrivial phase is accompanied by the closure and reopening of the gap

in the bulk spectrum of the superconducting wire. As shown in [28], this effect can also be observed in transport by measuring a nonlocal signal in the three-contact normal metal/superconducting wire/normal metal structure. It is assumed that the middle contact is created by the direct (not through a capacitor) grounding of a massive superconductor, which interact with the wire with a length of L. If $L \gg \xi$, the transport of quasiparticles with energies $E < \Delta_{eff}$, where Δ_{eff} is the gap in the bulk spectrum, between normal metal contacts will be suppressed due to the damping character of quasiparticle wavefunctions. We emphasize that it is taken into account that the gap Δ_{eff} in this case is effective, i.e., is determined not only by Δ but also by h and α [29]. In turn, at $\Delta_{eff} < E < \Delta_0$, where Δ_0 is the gap in the parent superconductor, a change in the current in the right contact I_2, which is due to a change in the voltage in the left contact V_1, i.e., the nonlocal conductance $G_{21} = dI_2/dV_1$, will be nonzero because of the normal transport of electrons or the transport of holes (the latter is caused by crossed Andreev reflection). Consequently, the only scenario for the appearance of a nonzero signal at $V = 0$ is the closure of the gap in the bulk spectrum at $h = h_c$ [11, 12, 30]. It is found that $G_{21}(V) = -G_{21}(-V)$ in this case; i.e., the current rectification $I \sim V^2$ is observed near the topological phase transition. The parameter Δ_{eff} at $h > h_c$, which can be estimated from the measured nonlocal conductance, is called the topological gap.

Using the described local and nonlocal measurement data, the authors of recent comprehensive study [31] attempted to plot a diagram of topological phases of a superconducting wire. The studied sample was a quasi-one-dimensional electron gas channel formed under the action of gate electrodes on the two-dimensional electron gas in an InAs quantum well. An aluminum stripe was epitaxially grown over the channel. The magnetic field was applied along the channel. Measurements showed that regions at the boundaries of which a gapless bulk spectrum is observed and the bulk spectrum with a gap occurs inside and outside of them exist in the V_g–B parametric space, where V_g is the gate voltage controlling the electron density in the channel and B is the magnetic field strength. In turn, conductance peaks of the left and right contacts at zero voltage simultaneously exist only inside islands. These resonances are stable under the variation of the height of tunnel barriers, the electron density, and the magnetic field. However, these regions are very small ($V_g \sim 1$ mV, $B \sim 100$ mT; i.e., $eV_g \sim 1$ meV, $h \sim 10$ μeV), and the topological gap $\Delta_{eff} = 20$–60 μeV is an order of magnitude smaller than the theoretically calculated values.

An important factor significantly complicating the interpretation of the results obtained in [31] and in other works in this field [32, 33] is very strong disorder in the studied hybrid samples [34–36]. Several scenarios are possible [37]. The first one is the inhomogeneity of the electrostatic potential, which is due to the presence of a set of gate electrodes necessary for controlling both the carrier density in the superconducting wire and height of tunnel barriers, charged impurities in the environment, and Schottky barriers [38]. As a result, the chemical potential can be considered as a smooth function of the coordinate both at the interface between the superconducting wire and the normal metal contact (quantum dot region can be formed here) [16, 32, 39, 40] and in the bulk of the wire [41]. In this case, ASs can appear in the trivial phase and have zero energy at certain parameters [2, 42, 43]. As a result, the conductance of the normal metal/superconducting wire interface at zero voltage is also equal to $2G_0$. Depending on the characteristics of the smooth inhomogeneity, the Majorana wavefunctions constituting such ASs can also be partially separated in space (such states are also referred to as quasi-MSs). Thus, their local linear response, i.e., $G_{11} = \left.\frac{dI_1}{dV_1}\right|_{V_1 \to 0}$, and its properties will much repeat those observed for MSs [44–46].

The second scenario is disorder and numerous impurities in the semiconductor core and at the semiconductor/superconducting shell interface, which can totally be interpreted as fluctuations of the electrostatic potential in the superconducting wire. Since the time-reversal symmetry in the system is broken ($h \neq 0$) and, as mentioned above, p-wave pairing dominates in the topologically nontrivial phase, disorder can be of great significance in contrast to the Bardeen–Cooper–Schrieffer superconductivity [47]. Majorana states in sufficiently large systems are stable under the effect of weak disorder (are topologically protected) due to their spatial nonlocality and to the gap in the spectrum of excitations [48, 49]. Strong disorder suppresses this gap and leads to the transition to the topologically trivial phase [50–52]. The decrease in the topological gap with increasing disorder will result in the significant hybridization of Majorana modes and again in the appearance of ASs whose energy can randomly vanish. As in the first scenario, strong disorder can also induce such ASs and ASs with partially separated Majorana modes in the trivial phase [34, 53]. It was shown that the response of these excitations is significantly similar to that of the true MS [54–56]. It is interesting that ASs with zero energy can also appear at $h = 0$, which can be used to estimate the degree of disorder in the system in experiments [37, 57].

We emphasize that rather short sample with a length of ~1 μm are used in current experiments in order to suppress the negative effect of disorder and to reach the ballistic transport regime [31, 36]. As a result, ASs appearing in both scenarios can have a nonzero probability density near the opposite boundaries of the hybrid structure [57]. Correspondingly, the

correlated behavior of local conductances G_{11} and G_{22}, which is characteristic of the resonant transport through the MS, can also be observed in the case of trivial quasiparticles [37, 46].

Besides the obvious necessity of reducing the degree of disorder in InAs/Al and InSb/Al hybrid structures, another possible solution to this problem is the search for alternative materials. Interest in lead tellurite PbTe has been significantly grown in recent time [58]. As InAs and InSb, PbTe wires have a strong spin–orbit coupling and a high g-factor [59, 60], but they also have a very high dielectric constant of $\sim 10^3$ [61], cf. ~10 in InAs and InSb [62]. Therefore, the efficient screening of charged impurities and a weaker disorder can be expected in this semiconductor. To protect PbTe wires from the formation of oxide layers on their surfaces (which are also sources of disorder), they are additionally coated with a CdTe film having the lattice matched to PbTe. For the same reason, PbTe wires are grown on CdTe substrates [63, 64]. The further development of the selective area growth of wires using molecular beam epitaxy allowed the improvement of the quality of interfaces [65]. As a result, the ballistic transport in zero magnetic field and, consequently, quantized conductance steps were observed [66, 67]. The length of the transport channel thus obtained can reach 1.5 μm, which is a factor of 1.5 to 10 larger than in InAs and InSb [68, 69].

The calculations showed that PbTe/Pb hybrid superconducting structures are promising and have some advantages [59]. The superconducting gap in lead is wider than that in aluminum; correspondingly, higher magnetic fields can be used in experiments. The superconducting gap in PbTe/Pb, which is comparable with those in InAs/Al and InSb/Al, can be induced even at a weak coupling between Pb and PbTe, which makes it possible to simultaneously reduce negative effects of renormalization and superconductor-induced disorder in the semiconductor. As mentioned above, a PbTe wire can first be coated with a CdTe buffer layer and a Pb film can then be grown or used as a layer coating PbTe/Pb. This allows one to solve the problems of mismatch between the PbTe and Pb lattices and the formation of oxide layers, which are significant sources of disorder. Recent experimental data have confirmed the solid (i.e., without parasitic quasiparticle states inside) induced gap $\Delta \sim 1$ meV [70], which is about five times wider than the known values in Al [19, 71].

The study of interference structures containing superconducting wires is of interest for two main reasons. First, because of the aforementioned problem of distinguishing between the responses of MSs and ASs (which are due to different mechanisms), it is necessary to use more complicated transport schemes [72–74]. Second, a number of theoretical works demonstrated that braiding of Majorana modes, which is necessary in the case of topological qubits to implement quantum gate operations, in systems with several ways is possible with measurements and the quantum teleportation effect (i.e., without any physical transport of modes) [75–77].

The Aharonov–Bohm effect, i.e., oscillations of the conductance as a function of the magnetic field perpendicular to the plane of the interference structure, is one of the criteria of the implementation of the coherent transport regime [78, 79]. Such a behavior of the differential conductance has been already demonstrated in practice for devices based on InSb [80] and PbTe [64]. An attempt to implement a MS in one of the arms of the interferometer was done in the experiment reported in [81]. However, the observed Aharonov–Bohm oscillations could not be attributed to the transport through separated Majorana modes and the possible contribution from bulk ASs (i.e., Bogoliubov excitations with strongly overlapping Majorana modes) could not be excluded.

It is shown below how the problem of distinguishing the response of the true MS from the responses of inhomogeneous and bulk ASs can be solved by analyzing features of the low-energy transport in the Π-shaped interference device [74, 82].

2. TRANSPORT PROPERTIES OF AN INHOMOGENEOUS INTERFEROMETER WITH A TOPOLOGICAL SUPERCONDUCTOR

We consider the steady-state current in the system that is shown in Fig. 1 and is described by the Hamiltonian

$$\hat{H} = \hat{H}_C + \hat{H}_D + \hat{H}_T. \tag{4}$$

Here, the first term $\hat{H}_C$ describes a single-band paramagnetic contact and has the form

$$\hat{H}_C = \sum_{k\sigma}\left(\xi_k - \frac{eV}{2} - \mu\right)c^+_{k\sigma}c_{k\sigma}, \tag{5}$$

where V is the bias voltage, μ is the chemical potential, $c_{k\sigma}$ is the annihilation operator for an electron with the wave vector k, spin σ, and energy ξ_k.

The next terms of the Hamiltonian are described in the tight-binding representation. However, it is noteworthy that, since the characteristic distances at which the wavefunctions of Majorana modes vary in superconducting wires are much larger than interatomic distances, the continuum approach can also be successfully applied to analyze the spectral and transport properties of such systems [30, 83, 84]. The second term is the Hamiltonian of the Π-shaped inhomogeneous interference device, which includes the superconducting segment S between two normal metal arms 1 and 2. In the tight-binding approximation and Nambu operator representation on the jth site

$\Psi_j = (a_{j\uparrow}\ a^+_{j\downarrow}\ a_{j\downarrow}\ a^+_{j\uparrow})^T$, the Hamiltonian of the structure has the form

$$\hat{H}_D = \sum_j \Psi^+_j [(V_j - \mu)\hat{\tau}_z - h_j\hat{\sigma}_x + \Delta_j\hat{\tau}_x]\Psi_j \qquad (6)$$

$$-\frac{1}{2}[\Psi^+_j (t - i\alpha_j(\hat{\sigma}_x\cos\varphi_j + \hat{\sigma}_y\sin\varphi_j))\hat{\tau}_z\Psi_{j+1} + \text{H.c.}].$$

Here, V_j is the electrostatic potential, h_j is the Zeeman splitting, Δ_j is the s-wave superconducting pairing potential, α_j is the spin–orbit coupling constant, θ_j is the angle at which the Rashba field is rotated at the motion from one segment to another, t is the hopping parameter between the sites of the device, and $\hat{\sigma}_i, \hat{\tau}_i$ ($i = x, y, z$) are the Pauli matrices acting in the spin and electron–hole spaces, respectively. The spatial dependences are specified by the expressions

$$V_j = \frac{e_1 + e_2}{2} + \frac{e_S - e_1}{2}\tanh\left(\frac{j - N_1}{\sigma_1}\right) - \frac{e_S - e_2}{2}\tanh\left(\frac{j - N_1 - N_S}{\sigma_2}\right), \qquad (7)$$

$$\Delta_j = \frac{\Delta}{2}\left[\tanh\left(\frac{j - N_1}{\sigma_1}\right) - \tanh\left(\frac{j - N_1 - N_S}{\sigma_2}\right)\right], \qquad (8)$$

$$h_j = h\Delta\theta_{S,j}, \quad \varphi_j = \frac{\pi}{2}\Delta\theta_{S,j}, \quad \alpha_j = \sum_{n=1,2,S}\alpha_n\Delta\theta_{n,j}, \qquad (9)$$

where e_1, e_2, and e_S are the on-site energies of the electron in subsystems 1, 2, and S, respectively, indicated in Fig. 1; N_1 and N_S are the numbers of sites in the normal metal arms and superconducting segments, respectively; σ_1 and σ_2 are the parameters specifying the degree of smoothness of the profiles at the N1/S and S/N2 interfaces, respectively; h is the Zeeman energy; Δ is the superconducting gap; α_1, α_2, and α_S are the spin–orbit coupling constants in the arms and superconducting wire, respectively; and $\Delta\theta_{S,j}$ and $\Delta\theta_{n,j}$ are expressed in terms of the Heaviside step function θ as

$$\Delta\theta_{1,j} = \theta(j-1) - \theta(j - N_1 - 1),$$
$$\Delta\theta_{2,j} = \theta(j - N_1 - N_S - 1) - \theta(j - 2N_1 - N_S - 1),$$
$$\Delta\theta_{S,j} = \theta(j - N_1 - 1) - \theta(j - N_1 - N_S - 1).$$

It is worth noting that the local character of the exchange field, which acts only in the superconducting wire, can be reached in practice due to the proximity effect by the deposition of the magnetic insulator film additional to the superconductor layer on the semiconductor core [20–22]. The superconducting wire is in the nontrivial phase in the Zeeman energy range $h_{c1} < h < h_{c2}$, where $h_{c1,2} = \sqrt{\Delta^2 + (e_S - \mu \mp t)^2}$. The wavefunctions of the Majorana modes composing the MS can penetrate into the normal metal arms and thus become available for interference measurements [30, 85, 86].

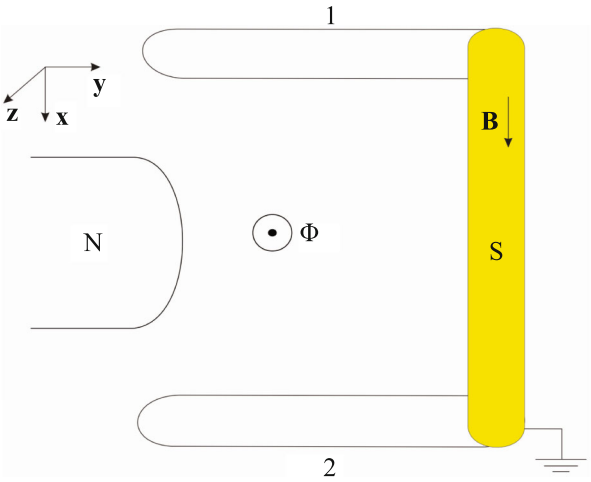

Fig. 1. (Color online) Π-shaped structure (interference device) interacting with the normal metal contact N. The device is a wire with the spin–orbit coupling, where superconducting pairing and Zeeman splitting are induced in the central segment (shown in yellow) due to proximity effects. The tunneling of carriers from arms 1 and 2 to the contact is accompanied by the appearance of the Aharonov–Bohm phase due to the magnetic flux Φ.

The last term in the Hamiltonian given by Eq. (4) describes the processes of tunneling between the normal metal contact and the arms of the device and has the form

$$\hat{H}_T = -\Psi^+_k\hat{\tau}_z(\hat{t}_1\hat{\Phi}\Psi_1 + \hat{t}_2\hat{\Phi}^+\Psi_L) + \text{H.c.}, \qquad (10)$$

where the matrices

$$\hat{t}_{1(2)} = \text{diag}(t_{1(2)\uparrow}, t^*_{1(2)\downarrow}, t_{1(2)\downarrow}, t^*_{1(2)\uparrow})$$

include tunneling parameters into the arms $t_{1,2\sigma}$ and the matrix

$$\hat{\Phi} = \text{diag}\left(e^{i\frac{\phi}{2}}, e^{-i\frac{\phi}{2}}, e^{i\frac{\phi}{2}}, e^{-i\frac{\phi}{2}}\right)$$

is determined by the Aharonov–Bohm phase $\phi = 2\pi\Phi/\Phi_0$, which appears at tunneling due to the magnetic flux Φ through the device plane; $\Phi_0 = h/e$ is the normal flux quantum.

The further numerical calculations were conducted with the parameters $t = 1$, $\mu = 0$, $e_1 = -0.1$, $e_2 = -0.5$, $e_S = 1.4$, $\alpha_1 = -\alpha_2 = 0.3$, $\alpha_S = 0.2$, $\Delta = 0.3$, $\sigma_1 = 3$, $\sigma_2 = 4$, $N_1 = 50$, and $N_S = 60$.

The presence of the electrostatic and superconducting pairing potentials smoothly varying near the interfaces allows the implementation of various low-energy states, which are distinguished in the spatial behavior of the wavefunctions of Majorana modes.

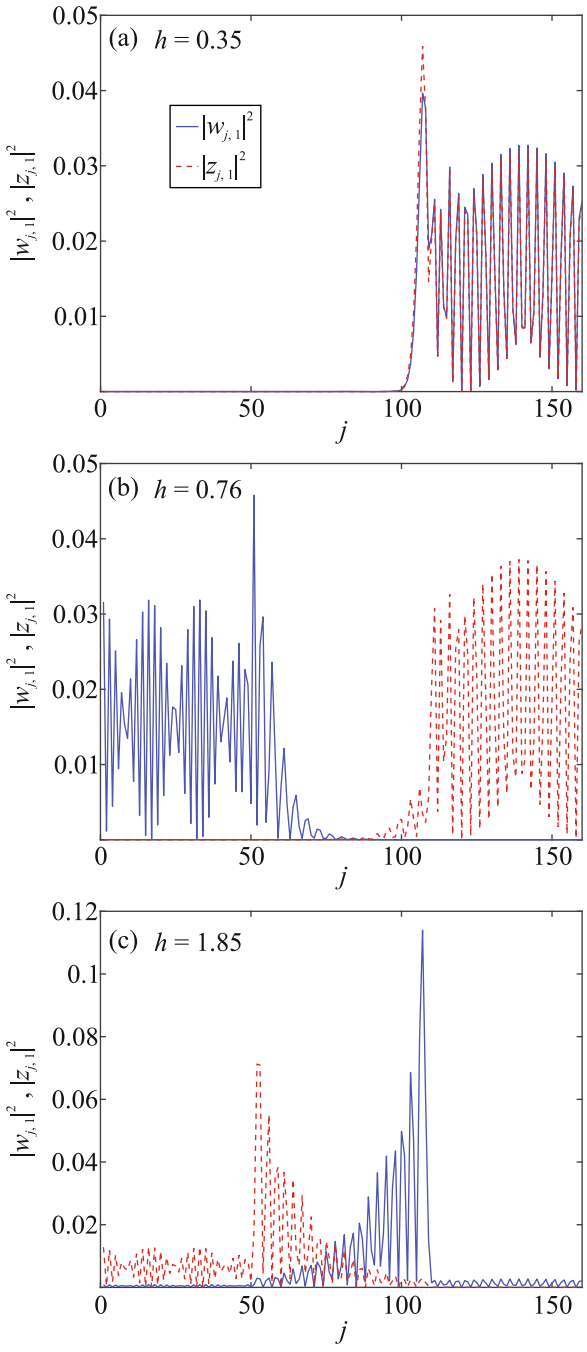

Fig. 2. (Color online) Spatial distribution of the probability densities $|w_{j,1}|^2$ and $|z_{j,1}|^2$ corresponding to the Majorana wavefunctions for three types of low-energy excitations of the interference device: (a) inhomogeneous Andreev state, (b) Majorana state, and (c) bulk Andreev state. The region $51 < j \le 110$ corresponds to the superconducting wire.

The spatial distributions of the corresponding probability densities $|w_{j,1}|^2$ and $|z_{j,1}|^2$ are presented in Fig. 2. The region $51 < j \le 110$ corresponds to the superconducting wire, and the left ($1 \le j \le 50$) and right ($110 < j \le 160$) segments belong to arms 1 and 2, respectively.

As known, in the Majorana-type Bogoliubov excitation, the wavefunctions of the Majorana modes corresponding to the operators $b_{1,1}$ and $b_{2,1}$ (see Eq. (2)) are localized at the opposite ends of the superconducting wire. In our case, as shown in Fig. 2b, these modes (probability densities are presented by the solid and dashed lines) outflow into adjacent arms; i.e., $|w_{j<51,1}|^2 \neq 0$ and $|z_{j>110,1}|^2 \neq 0$. It is substantial that excitations with a nearly zero energy can naturally appear in the considered inhomogeneous system, but they are not Majorana states (this possibility in a simpler case was demonstrated, e.g., in [38]). The wavefunctions of Majorana modes forming such states can significantly overlap with each other and can be localized in a limited spatial region. Such an inhomogeneous AS is exemplified in Fig. 2a. It is seen that both Majorana modes in this case are located in arm 2 ($j > 110$) and in the adjacent region of the superconductor. The excitation with the nearly zero energy, where the wavefunctions of Majorana modes strongly overlap with each other and have a nonzero probability density in the entire device is also possible, e.g., at a large Zeeman splitting for the superconducting wire that is formally in a topologically nontrivial phase ($h \lesssim h_{c2}$) [87]. The bulk AS is exemplified in Fig. 2c. It is noteworthy that $|z_{j,1}|^2$ (dashed line) and $|w_{j,1}|^2$ (solid line) are nonzero in arms 2 ($j > 110$) and 1 ($j < 51$), respectively, despite the visual effect. This is of fundamental significance for the interference transport.

The transport properties of the inhomogeneous superconducting device, which is simulated by the microscopic Hamiltonian given by Eq. (6), can be analyzed using the nonequilibrium Green's function method [88, 89] in the tight-binding approximation (details of the approach for the superconducting system can be found, e.g., in [90, 91]). Figure 3 presents the dependences of the conductance $G = dI/dV$ on the Aharonov–Bohm phase ϕ in the linear response regime at low temperatures. At $h < h_{c1} = 0.5$, oscillations of the differential conductance are shown by the solid line. They are due to the presence of one low-energy inhomogeneous AS in each of the opposite arms (one of such ASs is given in Fig. 2a). To observe the Aharonov–Bohm effect in this case, the energies of both inhomogeneous ASs ε_1 and ε_2 should be lower than or about the spin-dependent broadening parameters, which determine the lifetimes $\Gamma_{i\sigma}$, $i = 1, 2, 3, 4$, of four Majorana modes (two for each inhomogeneous AS). Moreover, according to analytical results obtained in [74] for the effective Hamiltonian of the two-level system (Andreev double-quantum-dot model), the dependence $G(\phi)$ occurs only if all four Majorana modes interact with the contact. It is seen in

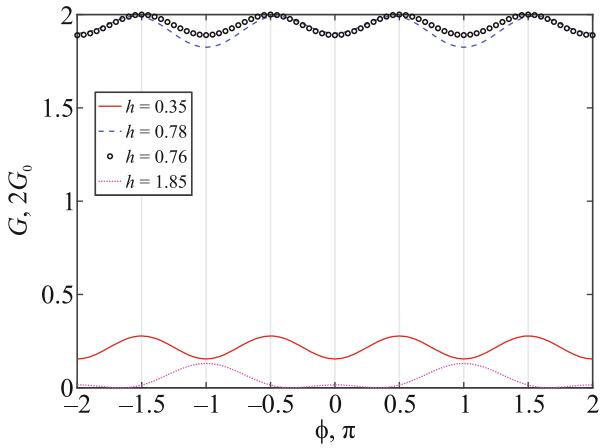

Fig. 3. (Color online) Aharonov–Bohm effect $G(\phi)$ at various Zeeman splitting magnitudes h.

Fig. 3 that the period of oscillations is π and extrema are at the points $\phi = \pi n/2$, $n \in \mathbb{Z}$.

Immediately above the topological phase transition point $h = h_{c1}$, the MS has zero energy $\varepsilon_1 = 0$. Further, since the Majorana wavefunction in the nontrivial phase demonstrates oscillations damping in the bulk of the superconducting wire and the localization length is inversely proportional to the gap in the bulk spectrum, the energy ε_1 undergoes oscillations increasing with the Zeeman energy h [87]. Although two Majorana modes of the lower excitation are already sufficient to observe the Aharonov–Bohm effect (as clearly seen in Fig. 2b), the cases with $\varepsilon_1 = 0$ and $\varepsilon_1 \neq 0$ differ in the properties of the effect and are shown in Fig. 3 by circles and the dashed line, respectively. Extrema in both cases are at the points $\phi = \pi n/2$. However, the period of oscillations in the more general situation with $\varepsilon_1 \neq 0$ is 2π.

At large Zeeman splitting, the MS is transformed to the bulk AS [92]. In this case, oscillations have a period of 2π and extrema both at $\phi = \pi n$ and between half-integer values of the Aharonov–Bohm phase. It is substantial that the latter values depend on the parameters of the system, whereas maxima and minima at integer ϕ values are stable. The revealed features of the conductance behavior in the effective model appear when the interaction of each of the Majorana modes with the contact simultaneously through both arms of the device is taken into account [74].

It is important that the Byers–Yang theorem [93] can be violated in mesoscopic superconducting structures. In particular, in one-dimensional and quasi-one-dimensional rings of *s*-wave superconductors, where the coherence length is smaller than or about the circle length, $\xi \sim L$, the critical temperature and supercurrent as functions of the magnetic flux have a period of 2π (i.e., a period of h/e inherent in normal metal systems) [94–97]. The period of conductance oscillations for the bulk AS in the considered system is doubled just at $\xi \sim N_S$. A period of $h/(2e)$ characteristic of extended superconducting systems occurs in the MS at any $\forall\varepsilon_1$ values if at least one of the two Majorana modes of the state with the energy ε_2 is localized near the N1/S or S/N2 interface and is no longer coupled to the contact (which can be ensured by increasing one of the parameters σ_1 and σ_2 [44, 74]).

Thus, considering the period of oscillations and the positions of the extrema of the conductance in the Aharonov–Bohm effect that are stable under the variation of the parameters of the system, one can distinguish the cases of the quantum interference transport in the MS, inhomogeneous ASs, and the bulk AS. This conclusion remains valid at nonzero temperatures $T \sim 10$ mK corresponding to experimental temperatures and including weak diagonal disorder [74].

Conductance maxima of $4G_0$ (the case of the MS in Fig. 3) indicate the transport involving simultaneously two Majorana modes [45]. If the coupling of the second mode with the contact is negligibly weak, peaks reach $2G_0$ [23, 24]. Two-channel interference can also be destructive, leading to $G = 0$. Both features are clearly seen in a particular case where one of the Majorana modes in the state with the minimum energy in a nontrivial phase does not outflow to the arm of the device adjacent to the superconducting wire. The dashed line in Fig. 4a is the dependence of the probability density of the second Majorana mode on the Zeeman energy $|z_{N,1}(h)|^2$ on the lower edge of the device ($N = 2N_1 + N_S$ is the number of sites in the interference structure). The coupling of this Majorana mode to the contact through the lower arm is obviously absent in both phases of the superconducting wire. The interaction is possible only through the upper arm, as seen in the behavior of $|z_{1,1}(h)|^2$ shown by the solid line. The probability density at the upper edge is maximal in the trivial phase ($h < 0.4$). However, since $\varepsilon_1 \gg \Gamma_{2\sigma}$, no resonant features of the conductance are observed (see the solid line in Fig. 4b). A sharp drop of $|z_{1,1}|^2$ occurs in the nontrivial phase near the threshold energy h_{c1}. In the case $N_S = 60$, this is insufficient to completely block the transport to the second Majorana mode (although certainly $\Gamma_{1\sigma} \gg \Gamma_{2\sigma}$), which is confirmed by the absence of the quantized conductance plateau [3]. As h increases, resonances in G alternate with antiresonances, where $G = 0$ ($h > 0.5$). In this case, the higher the density $|z_{1,1}|^2$, the higher the resonant G values above $2G_0$.

An increase in the length of the superconducting wire can ensure the exclusion of the second Majorana mode from transport processes. As a result, the conductance demonstrates a plateau with a height of $2G_0$ in the Zeeman energy range $0.4 < h < 0.6$ shown by the dashed line in Fig. 4b. The subsequent increase in h

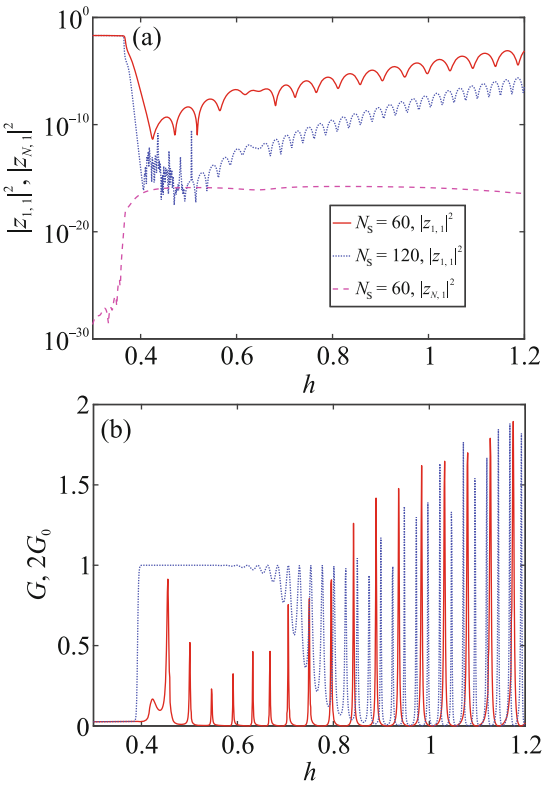

Fig. 4. (Color online) Case of the blocked transport to the lower arm at $\mu \approx 0.6$. (a) Probability density of the second Majorana excitation mode with the energy ε_1 at the upper edge of the device $|z_{1,1}|^2$ versus the Zeeman splitting h at $N_S =$ (solid line) 60 and (dashed line) 120. At the lower edge, $|z_{N,1}|^2 = 0$ for any h value (dashed line). (b) Conductance versus the Zeeman splitting h.

first leads to the increase in the hybridization of two Majorana excitation modes with the energy ε_1, which results in oscillations of the conductance with maxima of $2G_0$. Further, when the direct tunneling into the second Majorana mode becomes possible, the minima again reach zero and the maxima increase above $2G_0$, approaching $4G_0$.

3. CONCLUSIONS

Despite a significant progress in the synthesis of hybrid semiconductor/superconductor wires, the existing spectroscopic data are insufficient to indicate the presence of the Majorana state in these systems. One of the main obstacles to detect Majorana quasiparticles is disorder, which results in the appearance of low-energy Andreev states, whose transport responses are similar to that of Majorana excitations. This problem can be solved by the fabrication of purer InAS/Al and InSb/Al samples, which are studied since the first experiments to date, with $L > \xi$ and the synthesis of new hybrid wires, e.g., PbTe/Pb, where a semiconducting core has a large dielectric constant.

Differences between Majorana and Andreev states can be revealed in complex transport geometries. In particular, this problem is solved when examining the Aharonov–Bohm effect in an interference device with a superconducting segment in the central part. The identified differences are due to the features of the spatial behavior of Majorana modes, which constitute low-energy Bogoliubov states. The analysis of oscillations of the conductance as a function of the magnetic flux, as well as the positions of extrema in this dependence, allows one to separate the response of Majorana quasiparticles against the background of other Andreev states.

FUNDING

This work was supported by the Foundation for the Advancement of Theoretical Physics and Mathematics BASIS and in part by the Ministry of Science and Higher Education of the Russian Federation (state assignment for the Kirensky Institute of Physics, Federal Research Center KSC, Siberian Branch, Russian Academy of Sciences).

CONFLICT OF INTEREST

The author of this work declare that he has no conflicts of interest.

REFERENCES

1. A. Yu. Kitaev, Phys. Usp. **44**, 131 (2001).
2. A. F. Andreev, Sov. Phys. JETP **22**, 455 (1966).
3. V. V. Valkov, M. Shustin, S. Aksenov, A. Zlotnikov, A. Fedoseev, V. Mitskan, and M. Kagan, Phys. Usp. **65**, 2 (2022).
4. P. Marra, J. Appl. Phys. **34**, 124001 (2022).
5. A. Yu. Kitaev, Ann. Phys. **303**, 2 (2003).
6. C. Nayak, S. H. Simon, A. Stern, M. Freedman, and S. Das Sarma, Rev. Mod. Phys. **80**, 1083 (2008).
7. J. Alicea, Y. Oreg, G. Refael, F. von Oppen, and M. P. A. Fisher, Nat. Phys. **7**, 412 (2011).
8. D. A. Ivanov, Phys. Rev. Lett. **86**, 268 (2001).
9. E. Prada, R. Aguado, and P. San-Jose, Phys. Rev. B **96**, 085418 (2017).
10. M.-T. Deng, S. Vaitiekenas, E. Prada, P. San-Jose, J. Nygard, P. Krogstrup, R. Aguado, and C. M. Marcus, Phys. Rev. B **98**, 085125 (2018).
11. R. M. Lutchyn, J. D. Sau, and S. Das Sarma, Phys. Rev. Lett. **105**, 077001 (2010).
12. Y. Oreg, G. Refael, and F. von Oppen, Phys. Rev. Lett. **105**, 177002 (2010).
13. B. Braunecker, G. I. Japaridze, J. Klinovaja, and D. Loss, Phys. Rev. B **82**, 045127 (2010).
14. M. S. Shustin and S. V. Aksenov, J. Exp. Theor. Phys. **135**, 500 (2022).
15. J. Alicea, Rep. Prog. Phys. **75**, 0765017 (2012).

16. V. Mourik, K. Zuo, S. M. Frolov, S. R. Plissard, E. P. A. M. Bakkers, and L. P. Kouwenhoven, Science (Washington, DC, U. S.) **336**, 1003 (2012).
17. M. T. Deng, C. L. Yu, G. Y. Huang, M. Larsson, P. Caroff, and H. Q. Xu, Nano Lett. **12**, 6414 (2012).
18. A. Das, Y. Ronen, Y. Most, Y. Oreg, M. Heiblum, and H. Shtrikman, Nat. Phys. **8**, 887 (2012).
19. R. M. Lutchyn, E. P. A. Bakkers, L. P. Kouwenhoven, P. Krogstrup, C. M. Marcus, and Y. Oreg, Nat. Rev. Mater. **3**, 52 (2018).
20. S. Vaitiekenas, Y. Liu, P. Krogstrup, and C. M. Marcus, Nat. Phys. **17**, 43 (2021).
21. A. Maiani, R. Seoane Souto, M. Leijnse, and K. Flensberg, Phys. Rev. B **103**, 104508 (2021).
22. S. Vaitiekenas, R. S. Souto, Y. Liu, P. Krogstrup, K. Flensberg, M. Leijnse, and C. M. Marcus, Phys. Rev. B **105**, L041304 (2022).
23. K. T. Law, P. A. Lee, and T. K. Ng, Phys. Rev. Lett. **103**, 237001 (2009).
24. K. Flensberg, Phys. Rev. B **82**, 180516(R) (2010).
25. D. Rainis, L. Trifunovic, J. Klinovaja, and D. Loss, Phys. Rev. B **87**, 024515 (2013).
26. A. F. Andreev, Sov. Phys. JETP **19**, 1228 (1964).
27. J. J. He, T. K. Ng, P. A. Lee, and K. T. Law, Phys. Rev. Lett. **112**, 037001 (2014).
28. T. O. Rosdahl, A. Vuik, M. Kjaergaard, and A. R. Akhmerov, Phys. Rev. B **97**, 045421 (2018).
29. J. D. Sau, S. Tewari, R. M. Lutchyn, T. D. Stanescu, and S. Das Sarma, Phys. Rev. B **82**, 214509 (2010).
30. J. Klinovaja and D. Loss, Phys. Rev. B **86**, 085408 (2012).
31. M. Aghaee, A. Akkala, Z. Alam, et al., Phys. Rev. B **107**, 245423 (2023).
32. P. Yu, J. Chen, M. Gomanko, G. Badawy, E. P. A. M. Bakkers, K. Zuo, V. Mourik, and S. M. Frolov, Nat. Phys. **17**, 482 (2021).
33. Z. Wang, H. Song, D. Pan, Z. Zhang, W. Miao, R. Li, Z. Cao, G. Zhang, L. Liu, L. Wen, R. Zhuo, D. E. Liu, K. He, R. Shang, J. Zhao, and H. Zhang, Phys. Rev. Lett. **129**, 167702 (2022).
34. B. D. Woods, S. Das Sarma, and T. D. Stanescu, Phys. Rev. Appl. **16**, 054053 (2021)
35. S. Das Sarma, Nat. Phys. **19**, 165 (2023).
36. S. M. Frolov, P. Zhang, B. Zhang, Y. Jiang, S. Byard, S. R. Mudi, J. Chen, A.-H. Chen, M. Hocevar, M. Gupta, C. Riggert, and V. S. Pribiag, arXiv: 2309.09368 (2023).
37. H. Pan and S. Das Sarma, Phys. Rev. Res. **2**, 013377 (2020).
38. G. Kells, D. Meidan, and P. W. Brouwer, Phys. Rev. B **86**, 100503(R) (2012).
39. C. Liu, J. D. Sau, T. D. Stanescu, and S. Das Sarma, Phys. Rev. B **96**, 075161 (2017).
40. C.-X. Liu, J. D. Sau, and S. Das Sarma, Phys. Rev. B **97**, 214502 (2018).
41. C. Moore, C. Zeng, T. D. Stanescu, and S. Tewari, Phys. Rev. B **98**, 155314 (2018).
42. E. Prada, P. San-Jose, M. W. A. de Moor, A. Geresdi, E. J. H. Lee, J. Klinovaja, D. Loss, J. Nygard, R. Aguado, and L. P. Kouwenhoven, Nat. Rev. Phys. **2**, 575 (2020).
43. P. Marra and A. Nigro, J. Phys.: Condens. Matter **34**, 124001 (2022).
44. F. Penaranda, R. Aguado, P. San-Jose, and E. Prada, Phys. Rev. B **98**, 235406 (2018).
45. A. Vuik, B. Nijholt, A. R. Akhmerov, and M. Wimmer, SciPost Phys. **7**, 061 (2019).
46. R. Hess, H. F. Legg, D. Loss, and J. Klinovaja, Phys. Rev. B **104**, 075405 (2021).
47. P. W. Anderson, J. Phys. Chem. Solids **11**, 26 (1959).
48. J. D. Sau, S. Tewari, and S. Das Sarma, Phys. Rev. B **85**, 064512 (2012).
49. J. D. Sau and S. Das Sarma, Phys. Rev. B **88**, 064506 (2013)
50. O. Motrunich, K. Damle, and D. A. Huse, Phys. Rev. B **63**, 224204 (2001).
51. P. W. Brouwer, M. Duckheim, A. Romito, and F. von Oppen, Phys. Rev. B **84**, 144526 (2011).
52. P. W. Brouwer, M. Duckheim, A. Romito, and F. von Oppen, Phys. Rev. Lett. **107**, 196804 (2011).
53. S. Ahn, H. Pan, B. Woods, T. D. Stanescu, and S. Das Sarma, Phys. Rev. Mater. **5**, 124602 (2021).
54. D. Bagrets and A. Altland, Phys. Rev. Lett. **109**, 227005 (2012).
55. H. Pan, W. S. Cole, J. D. Sau, and S. Das Sarma, Phys. Rev. B **101**, 024506 (2020).
56. H. Pan and S. Das Sarma, Phys. Rev. B **105**, 115432 (2022).
57. P. Yu, B. D. Woods, J. Chen, G. Badawy, E. P. A. M. Bakkers, T. D. Stanescu, and S. M. Frolov, SciPost Phys. **15**, 005 (2023).
58. S. G. Schellingerhout, E. J. de Jong, M. Gomanko, X. Guan, Y. Jiang, M. S. M. Hoskam, S. Koelling, O. Moutanabbir, M. A. Verheijen, S. M. Frolov, and E. P. A. M. Bakkers, arXiv: 2110.12789 (2021).
59. Z. Cao, D. E. Liu, W.-X. He, X. Liu, K. He, and H. Zhang, Phys. Rev. B **105**, 085424 (2022).
60. M. Gomanko, E. J. de Jong, Y. Jiang, S. G. Schellingerhout, E. P. A. M. Bakkers, and S. M. Frolov, SciPost Phys. **13**, 089 (2022).
61. S. Yuan, H. Krenn, G. Springholz, Y. Ueta, G. Bauer, and P. J. McCann, Phys. Rev. B **55**, 4607 (1997).
62. G. W. Winkler, A. E. Antipov, B. van Heck, A. A. Soluyanov, L. I. Glazman, M. Wimmer, and R. M. Lutchyn, Phys. Rev. B **99**, 245408 (2019).
63. Y. Jiang, S. Yang, L. Li, et al., Phys. Rev. Mater. **6**, 034205 (2022).
64. Z. Geng, Z. Zhang, F. Chen, et al., Phys. Rev. B **105**, L241112 (2022).
65. W. Song, Z. Yu, Y. Wang, et al., arXiv: 2402.02132 (2024).
66. W. Song, Y. Wang, W. Miao, et al., Phys. Rev. B **108**, 045426 (2023).
67. Y. Wang, F. Chen, W. Song, et al., Nano Lett. **23**, 11137 (2023).
68. J. Gooth, M. Borg, H. Schmid, V. Schaller, S. Wirths, K. Moselund, M. Luisier, S. Karg, and H. Riel, Nano Lett. **17**, 2596 (2017).

69. J. Kammhuber, M. Cassidy, H. Zhang, Ö. Gül, F. Pei, M. W. A. de Moor, B. Nijholt, K. Watanabe, T. Taniguchi, D. Car, S. Plissard, E. Bakkers, and L. Kouwenhoven, Nano Lett. **16**, 3482 (2016).
70. Y. Gao, W. Song, S. Yang, et al., arXiv: 2309.01355 (2023).
71. W. Chang, S. Albrecht, T. Jespersen, F. Kuemmeth, P. Krogstrup, J. Nygard, and C. M. Marcus, Nat. Nanotechnol. **10**, 232 (2015).
72. K. M. Tripathi, S. Das, and S. Rao, Phys. Rev. Lett. **116**, 166401 (2016).
73. M. Hell, K. Flensberg, and M. Leijnse, Phys. Rev. B **97**, 161401(R) (2018).
74. S. V. Aksenov, Phys. Rev. B **107**, 085417 (2023).
75. P. Bonderson, M. Freedman, and C. Nayak, Phys. Rev. Lett. **101**, 010501 (2008).
76. L. Fu, Phys. Rev. Lett. **104**, 056402 (2010).
77. S. Vijay and L. Fu, Phys. Rev. B **94**, 235446 (2016).
78. Y. Aharonov and D. Bohm, Phys. Rev. **115**, 485 (1959).
79. S. Datta, *Electronic Transport in Mesoscopic Systems* (Cambridge Univ. Press, New York, 1995).
80. R. L. O. het Veld, D. Xu, et al., Commun. Phys. **3**, 1 (2020).
81. A. M. Whiticar, A. Fornieri, E. C. T. O'Farrell, A. C. C. Drachmann, T. Wang, C. Thomas, S. Gronin, R. Kallaher, G. C. Gardner, M. J. Manfra, C. M. Marcus, and F. Nichele, Nat. Commun. **11**, 3212 (2020).
82. S. V. Aksenov, J. Phys.: Condens. Matter **34**, 255301 (2022).
83. A. A. Kopasov and A. S. Mel'nikov, Phys. Rev. B **101**, 054515 (2020).
84. A. A. Kopasov, A. G. Kutlin, and A. S. Mel'nikov, Phys. Rev. B **103**, 144520 (2021).
85. D. Chevallier, D. Sticlet, P. Simon, and C. Bena, Phys. Rev. B **85**, 235307 (2012).
86. E. Vernek, P. H. Penteado, A. C. Seridonio, and J. C. Egues, Phys. Rev. B **89**, 165314 (2014).
87. S. Das Sarma, J. D. Sau, and T. D. Stanescu, Phys. Rev. B **86**, 220506(R) (2012).
88. L. V. Keldysh, Sov. Phys. JETP **20**, 1018 (1964).
89. P. I. Arseev, Phys. Usp. **58**, 1159 (2015).
90. V. V. Val'kov and S. V. Aksenov, J. Magn. Magn. Mater. **465**, 88 (2018).
91. V. V. Val'kov, M. Yu. Kagan, and S. V. Aksenov, J. Phys.: Condens. Matter **31**, 225301 (2019).
92. A. Haim, E. Berg, F. von Oppen, and Y. Oreg, Phys. Rev. Lett. **114**, 166406 (2015).
93. N. Byers and C. N. Yang, Phys. Rev. Lett. **7**, 46 (1961).
94. K. Czajka, M. M. Maska, M. Mierzejewski, and Z. Sledz, Phys. Rev. B **72**, 035320 (2005).
95. T.-C. Wei and P. M. Goldbart, Phys. Rev. B **77**, 224512 (2008).
96. V. Vakaryuk, Phys. Rev. Lett. **101**, 167002 (2008).
97. F. Loder, A. P. Kampf, and T. Kopp, Phys. Rev. B **78**, 174526 (2008).

Translated by R. Tyapaev